C h a p t e r   4

MODELING

4.1   Discrete particle model for the granular chain

We model the granular crystal as an array of masses and springs coupled by a nonlinear Hertzian contact law[22,93]. The Hertzian contact law defines the force, F, needed to achieve a certain overlap, δ, between two compressed spherical particles,

$$F = A\delta^{3/2}. \tag{4.1}$$

The Hertzian contact factor, A, is a function of spheres radii, R_i, Youngs modulus, E_i, and Poissons ratio, v_i, for the materials of the two particles, $A = \frac{4}{3}\left(\frac{1-v_i^2}{E_i} + \frac{1-v_j^2}{E_j}\right)^{-1}\left(\frac{R_iR_j}{R_i+R_j}\right)^{1/2}$. The exponent of 3/2 is caused by a geometric nonlinearity. At zero compression the spheres are in contact at a single point. However, as two particles are compressed, there is an increase in the contact surface area. This causes an increase in the incremental stiffness and results in the nonlinear force interaction[22,94].

4.1.1   Hamiltonian approximation

The complex features of wave propagation in an array of spherical particles can be greatly simplified by considering a simple mass spring model. Nesterenko first used this model in granular media to predict solitary waves[35], where the nonlinearity and dispersion necessary for the formation of these waves are provided by the nonlinear contact and the periodicity, respectively. Each point mass is equivalent to the mass of the spheres and the nonlinear

springs are described by the Hertzian force law. This allows us to write an equation of motion for each of the beads displacements (4.2), u_i, using Newton's second law for inertia, where each bead is subject to a force due to each adjacent bead[35],

$$m_i \ddot{u}_i = A_i \delta_i^{3/2} - A_{i+1} \delta_{i+1}^{3/2}, \tag{4.2}$$

where δ_i is the overlap of two adjacent beads and can be described in terms of their neighboring equilibrium positions and an initial static overlap, δ_0,

$$\delta_i = \delta_0 + u_{i-1} - u_i. \tag{4.3}$$

This discrete particle model seems like an oversimplification of the dynamics that occur in the real system but can be supported if each mass can be considered a point mass. The assumption is valid only as long as none of the internal resonances of the spheres are present. This is equivalent to having the spheres' first structural resonance frequency high above the dynamic range of interest. Below this frequency, the sphere moves as a rigid body and can be considered a point mass. It is important to check this assumption. When the internal resonance frequency of the single particle is low enough the internal resonances of the particle cannot be ignored. Interest in metamaterials in granular systems is based on this concept, in which materials gain remarkable properties by designing each periodic unit to have an internal resonant structure[49]. In fact, our study of tunable localized modes in periodic media relies on an internal resonance which interacts with the normal extended modes of the system.

4.1.2   Nonconservative elements

In our experiments the dynamics are not Hamiltonian, but are instead a driven damped system. This means that we need to add neoconservative terms to the Hamiltonian system presented above. To account for the damping that is inherently present in real systems we add a linear dissipative term, $m_i \dot{u}_i / \tau$, where τ is a linear dissipation time constant. This linear dissipation time constant can also be measured through a non-dimensional quality factor, $Q = \omega_0 \tau$, where ω_0 is the linear resonance frequency, or using the exponentially decaying envelope of the signal oscillation. In cases when there are mass defects and the dissipation of all the particles becomes important, it may be more appropriate to use a mass normalized dissipation, $b\dot{u}$, where $b = m_i / \tau$. This leads to a modified equation of motion,

$$m_i \ddot{u}_i = A_i \delta_i^{3/2} - A_{i+1} \delta_{i+1}^{3/2} + m_i \dot{u}_i / \tau . \qquad (4.4)$$

In order to include the non-conservative inputs signals, we consider the nature of the excitations. In our system all the excitations are provided by piezoelectric elements that are nearly two orders of magnitude stiffer than the Hertzian contact interaction. Therefore we assume that the piezoelectric actuator can expand freely, and that the excitation is a displacement controlled signal. To model this we modify the local overlap of the contacts,

$$\delta_i = B_i \cos \omega_d t + \delta_0 + u_{i-1} - u_i. \qquad (4.5)$$

This notation can be used to represent a moving wall or an expanding piezoelectric actuator between two particles, and has the effect of adding or removing energy from the system depending on the relative phases of the drive and particle motion.

4.2   Linear eigenanalysis and state space

Most of the dynamics that we explore are weakly nonlinear. It is therefore good to start by understanding the linearized system. By taking an appropriate linearization of the equations of motion (4.2), assuming oscillatory solutions for the particles, $u_i = e^{i\omega t}$, and ignoring dissipation, we can formulate an eigenvalue problem[70,95],

$$-i\omega^2 M\boldsymbol{u} = K\boldsymbol{u}, \tag{4.6}$$

where omega is the frequency of the oscillation, **M** is the diagonal mass matrix describing the system, and **K** is stiffness matrix describing the coupling between masses in the system. We can then solve this for the eigenvectors (normal modes) and eigenvalues (resonant frequencies) of the system. The extended normal modes of crystal are responsible for propagating wave energy at each of the frequencies. In the infinite system the solution can be found using Bloch conditions, which results in continuous frequency bands[95]. The linearized equations of motion for the granular crystal (4.6) are the same form of equations used to model the acoustic and optical bands for phonons in materials[95]. In finite systems the frequency bands are no longer continuous, but instead there are finite numbers of modes that lie along the continuous dispersion relation.

If dissipation and an excitation are included in the model we can also find a linear transfer function using state space analysis[31]. This numerical technique is a particularly fast and computationally inexpensive route to obtaining the linear response that corresponds to a particular experimental excitation and measurement arrangement. This allows us to numerically observe the band gaps that occur as a result of the periodicity of the lattice. In

addition, because our system has more than one degree of freedom and possibly different dissipation for each particle, fitting the dissipation of a single mode may not accurately represent the dissipation across the lattice. State space analysis can provide a powerful mechanism to fitting to different linear dissipation models.

4.3   Nonlinear modeling: integration and perturbation analysis

4.3.1   Integration

The equations of motion are inherently nonlinear, and therefore must be integrated if we want to predict any of the nonlinear dynamical phenomena. To integrate the equations of motion for n beads, we must transform the n 2nd order ODEs into a system of $2n$ first order ODEs[96]. The integration allows us to observe and predict bifurcation phenomena, transient dynamics, and mode bending. We use two integration schemes, either a 4th order Runge Kutta or the MATLAB ode45 function. For both integration schemes, it is essential to choose tolerances or time-steps that are small enough, ensuring that energy is conserved and/or that the integration captures the interested dynamics. Generally we use a time step of 50 ns in the 4th order Runge Kutta. In the matlab solvers, we use a relative tolerance of 1e-4 and an absolute tolerance of 1e-14. As solutions get close to bifurcation points, it may be necessary to significantly increase the accuracy by reducing the tolerance or integration time step.

4.3.2   Perturbation analysis for limit cycle solutions

A significant portion of this research involves studying the phenomena close to instability points or when dynamics are unstable and go through a bifurcation. In general the equations of motion can be recast into a system of 1st order ordinary differential equations of the form,

$$\dot{x} = h(x, \dot{x}, t) \tag{4.7}$$

where h is a vector function describing the dynamics of the evolution and x is the solution. In our case the equations depends on time because there is an external forcing. In the limit of small excitations, far from any bifurcations, the solution to our system is periodic with the same period of the excitation. Dissipation will cause any of the transient signals to decay and the steady state response will be at the excitation frequency. Therefore our system settles to a periodic orbit. Limit cycles are a closed periodic orbit in a systems phase space, and Floquet analysis is a tool that enables the study of the stability of limit cycle orbits. As the system's amplitude grows beyond the linear limit, nonlinearity grows in importance. The nonlinearity can cause the stable periodic solution to suddenly become unstable and result in a wealth of new dynamics. Floquet analysis can tell us the stability of the limit cycles and when a limit cycle becomes unstable, what new dynamics may appear. This tool is a linear perturbation analysis tool from the periodic limit cycle. It therefore also gives us insight into how fast the system reacts to perturbations[8,28].

Algorithm

Floquet analysis has been used in damped driven systems[28,29,97] and in granular crystals. Normally, one searches for both the period of the limit cycle and the limit cycle itself in phase space. One option to finding the a periodic orbit is to simply integrate the system for long times and wait for the system to approach a periodic attractor[97]. However this does not allow

convergence to the desired attractor and may take a long time. Since in a driven damped system the period may be known beforehand, we can also solve for the limit cycle (see Applied Nonlinear Dynamics Ch. 6.5.2 section on Nonautonomous Systems)[97]. A limit cycle can is defined as close periodic orbit, or equivalently,

$$x(T) = x^0,\tag{4.8}$$

where x^0 is the initial condition and T is the period. In Floquet Analysis, we are looking for a matrix that describes the perturbations to the initial condition that satisfies this relation. That is, we are looking to see how the solution one period later responds to a small change in the initial condition, x^0. This idea is embodied in a variational matrix, which describes how the sensitivity of the orbit on the choice of initial condition,

$$V(t) = \frac{\partial x(t)}{\partial x^0}.\tag{4.9}$$

When time equals that for a single period $t = T$, the variational matrix describes the deviation of the solution at full period later. This can be more easily envisioned in a two-dimensional system, schematically shown in Fig 4.1, in which the small deviation in the initial condition leads to a non-closed orbit after one period, T.
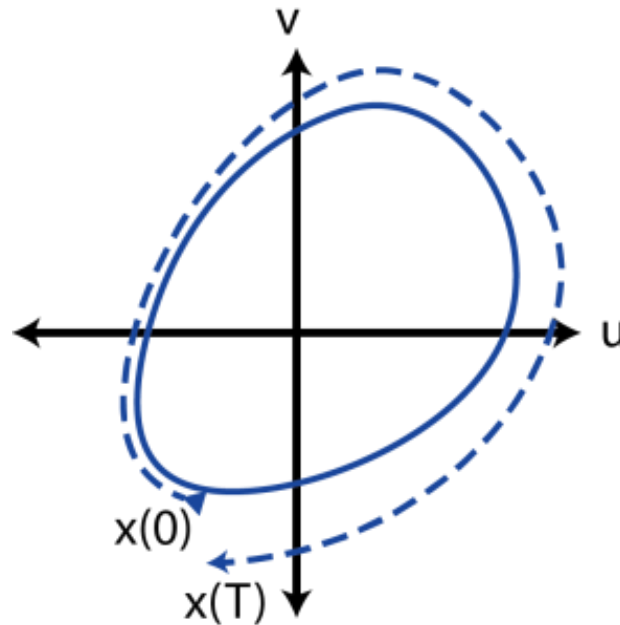
Figure 4.1: A schematic representation of a periodic orbit in a system with two degrees of freedom, position, and velocity. The solid line indicates a closed limit cycle orbit while the dotted line shows that changing the initial condition to a point slightly off the orbit results in a orbit that is not closed. The variational matrix, V, describes this sensitivity.

Since every orbit is not necessarily a closed orbit, and we do not know the initial condition that will provide a closed orbit, we must search for a closed orbit solution. This means finding a solution of map,

$$f(x^0) = x^0 - x(T) = 0. \tag{4.10}$$

The value $x(T)$ depends on the integration from the initial condition x^0. We begin with an initial guess and then modify that initial guess using Newton's Method until we find the solution that provides a closed orbit,

$$x_{i+1}^0 - x_i^0 = \left(J_n(x_i^0)\right)^{-1} f(x_i^0), \tag{4.11}$$

where x_i^0 is the approximation of the initial condition x^0 after i iterations. The Jacobian matrix, J_n, is for the defined for the function, f, and is

$$J_n = \frac{\partial f}{\partial x^0} = \frac{\partial}{\partial x^0}[x^0 - x(T)] = \left[I - \frac{\partial x(T)}{\partial x^0}\right] = I - V(T).$$

$$\tag{4.12}$$

$$J_n = I - V(T)$$

The Newtons method then becomes,

$$x_{i+1}^0 = x_i^0 + \left(I - V(T)\right)^{-1}\left(x^0 - x(T)\right) \tag{4.13}$$

which depends on both the solution of the system, $x(T)$, and the variational matrix, $V(T)$, after integrating for a full period. The equations to integrate for the system are defined by h. However, we need to define the evolution of the variational matrix,

$$\dot{V} = \frac{\partial}{\partial t}\frac{\partial x(t)}{\partial x^0} = \frac{\partial}{\partial x^0}\frac{\partial x(t)}{\partial t} = \frac{\partial}{\partial x^0} h(x(t), \dot{x}, t). \tag{4.14}$$

Since the system of ODE's h depend on $x(t)$, which definitely depends on the initial guess, we must apply chain rule,

$$\dot{V} = \left(\frac{\partial}{\partial x} h(x(t), \dot{x}, t)\right)\frac{\partial x}{\partial x^0}, \tag{4.15}$$

and the first factor in the product is simply the Jacobian of the system h, and the second factor in the product is the variational matrix itself. Therefore the time evolution of the variational matrix is

$$\frac{d}{dt}V = J_{sys}V .$$

(4.16)

Using this we can now perform the Newton method after integrating each initial guess for one full period.

Comments on the resolution and the algorithm tolerance

We integrate the ODE and search for the following condition numerically. However, there is inherently an error to the Newton method in solving this problem. Therefore, we stop the algorithm when the condition for the Newton method is below some tolerance.

$$f(x^0) = x^0 - x(T) < tol.$$

(4.17)

This defines the resolution and accuracy of the time periodic solution for which we are searching. When we are far from a bifurcation this tolerance can be relatively large since the system itself is stable. However, near a bifurcation the system is less stable, and perturbations have the tendency to grow. This means that for the algorithm to converge the tolerance of the integrator may need to be reduced. We typically look for solutions with a tolerance, $tol = 10^{-14}$, which should be compared with the static overlap of the system, $\delta_0 \approx 10^{-7}$.

Comments on the variational matrix

After integrating the variational matrix for a full period we find,

$$V(T) = \frac{\partial x(T)}{\partial x^0}.$$
(4.18)

When the system is on a limit cycle the initial condition and final state of the system are equivalent, $x(T) = x^0$. This means that the matrix tells us the linear sensitivity that a perturbation has on the final state, where the eigenvalues, λ_i, of V describe the growth of a perturbation in the associated eigenvector direction. The eigenvalues of the matrix are complex and give us information both about the stability of the limit cycle and when the limit cycle is stable, i.e., the speed of the system[8,97]. The magnitude of the eigenvalue, $|\lambda_i|$, dictates the growth rate of the perturbation, and the argument tells the frequency of the growing perturbation, $f_N = Arg(\lambda_i)/(2\pi T)$. When the system is Hamiltonian, multipliers sit on the unit circle in the complex plane. However, when the system is damped, as in our case, the multipliers lie on a circle of with a radius dependent upon the linear dissipation, $e^{-T/(2\tau)}$, where τ is a linear dissipation time constant[28]. This reflects the notion that transients decay in a dissipative system, and the rate of decay is dictated by this value. A perturbation acts as a small transient. Therefore, when the magnitudes of the multipliers are less than one, perturbations die, and the rate of the exponential approach back to the limit cycle is dictated by the magnitude of the Floquet multiplier. As the magnitude of this multiplier approaches unity, the time constant to return to the limit cycle approaches infinity. At the bifurcation point the time is infinite and the system is sitting on top of a saddle node. A small perturbation does not decay. Finally, when the magnitude is greater than one the perturbation grows exponentially and the limit cycle is not stable.

4.4   Modeling specific tools

4.4.1   Lock-in amplifier

We frequently connect the measureable experimental parameters to a lock-in amplifier. The measured variable could be the velocity of particle i, the force at the boundary, or the force in the middle of a bead. The lock-in amplifier multiplies the measured variable by the sine and cosine at the reference frequency, low pass filters the signal, and outputs the Fourier component of the measured variable at the reference frequency. This process can be modeled using a system of n first order ODEs, where n is the order of the low pass filter and τ is the time constant of the low pass filter of the lock-in amplifier. The ODE for measuring a variable, x_{input}, can be written as,

$$
\begin{aligned}
\dot{y}_1 &= x_{input} * \cos(\omega_{ref}t) - y_1 \\
\dot{y}_2 &= (y_1 - y_2)/\tau \\
&\cdots \\
\dot{y}_n &= (y_{n-1} - y_n)/\tau \\[6pt]
\dot{y}_{n+1} &= x_{input} * \sin(\omega_{ref}t) - y_{n+1} \\
\dot{y}_{n+2} &= (y_{n+1} - y_{n+2})/\tau \\
&\cdots \\
\dot{y}_{2n} &= (y_{2n-1} - y_{2n})/\tau.
\end{aligned}
\tag{4.19}
$$

This amplitude, A, and phase with respect to the excitation signal, ϕ, of the measured variable are described by the equations,

$$
\begin{aligned}
A &= 2\sqrt{y_n^2 + y_{2n}^2} \\
\phi &= \tan^{-1}\left(\frac{y_{2n}}{y_n}\right)
\end{aligned}
\tag{4.20}
$$

4.4.2   Embedded piezoelectric sensor

There has been extensive use of an embedded piezoelectric element for sensing purposes[31,32,68,77]. Two important considerations when using embedded piezoelectric sensors are the input impedance of the measurement device and the frequency of operation. When the impedance between the terminals is relatively large compared to the impedance of the piezo, the force and voltage can be proportionally related. The time constant of the piezoelectric measuring circuit is also important.   When using the piezo as a sensing device, the measurement frequency should always be well above the reciprocal of the time constant. If a low resistance is placed in parallel with the pizeo, this affects the time constant and accurate sensing is pushed to a higher frequency regime.

Studies on granular crystals have proposed their potential application in energy harvesting devices[98]. For this, the associated circuit and configuration becomes extremely important, and has previously been ignored. The goal is to convert mechanical energy into electrical energy, and therefore the electro mechanical coupling must be incorporated in the equations of motion for the mechanical and electrical systems. I present here equations of motion for the piezoelectric disk embedded in a sphere. These are more generally and do not make assumptions about small strains on the piezo, flat frequency response, or rigid body motion. These equations (or similarly derived depending on differing geometries) need to be checked when considering energy harvesting in a granular chain.

We use a Lagrangian approach, which allows us to derive equations of motion from the constitutive response of a piezoelectric disc and use generalized coordinates, so that the approach can be easily adopted for different circuits or mechanical geometries. The approach closely follows that presented by A. Preumon[99]. The constitutive laws of a piezoelectric disk

$$\begin{pmatrix} D \\ S \end{pmatrix} = \begin{bmatrix} \varepsilon^T & d_{33} \\ d_{33} & s^E \end{bmatrix} \begin{pmatrix} E \\ T \end{pmatrix},$$ (4.21)

can be integrated over the volume, inverted, and then used to define a coenergy function,

$$W_e^*(\Delta, \dot{\lambda}) = \frac{C(1-k^2)}{2} \dot{\lambda}^2 + n d_{33} K_a \dot{\lambda} \Delta - \frac{K_a}{2} \Delta^2 ,$$ (4.22)

where λ is the generalized coordinate, chosen as the flux linkage across the piezo. The other parameters follow correspond to coefficients as in Preumont's derivation[99] and the IEEE standards for piezoelectricity[100]. They are defined in the table.

ε^T	Permittivity	$k = \dfrac{d_{33}^2}{s^E \varepsilon^T}$	Electromechanical coupling factor
d_{33}	Piezoelectric Constant	$K_a = \dfrac{A}{s^E t}$	Short circuit stiffness
s^E	Compliance	t	Thickness
A	Area	$Q = AD$	Charge
D	Charge Displacement	$\Delta = St$	Total Displacement
S	Strain	$f = TA$	Force
T	Stress	$V = Et$	Voltage
E	Electric Field	$C = \dfrac{\varepsilon^T A}{t}$	Capacitance

Table 4.1: IEEE Notation for derivation of the electromechanical coupling for piezoelectric disks embedded between two half spheres.

The coenergy function can be included in the Lagrangian for the system as,

$$L = T - V + W_e^*,$$
(4.23)

where T is Kinetic energy and V is the Potential energy of the system. By defining a kinetic energy and a potential energy of the system presented in the figure below, we can then derive the equations of motion using Lagrange's equations.
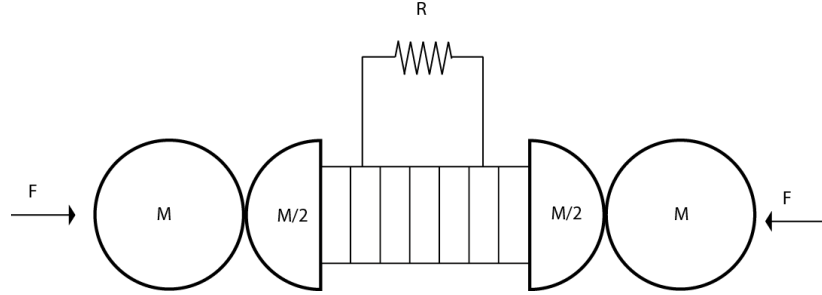

Figure 4.2: A schematic of the embedded piezoelectric element and connected circuit. Under certain conditions the electromechanical coupling can be ignored and we can assume voltage is proportional to the applied force[34]. However, in many applications such as energy harvesting, the dynamics of the electrical circuit becomes essential.

The figure shows two beads in contact with the central bead with the embedded piezoelectric disk. The coordinates of the two neighboring beads only enter in the equations of the potential of the system, since the equations of motion for these particles can be easily derived from Newtonian mechanics. This leads us to define the kinetic minus potential energy of the system as,

$$T - V = \frac{1}{2}\dot{u}_{2L}^2 + \frac{1}{2}\dot{u}_{2R}^2 - \frac{2}{5}A(\delta_0 - u_{2L} + u_1)^{\frac{5}{2}} - \frac{2}{5}A(\delta_0 - u_3 + u_{2R})^{\frac{5}{2}},$$
(4.24)

where u_1 and u_3 are the equilibrium positions of the two neighboring beads and u_{2L} and u_{2R} are the equilibrium position for the two half beads that are attached to the piezoelectric sensor.

The coenergy function for the piezo is defined above, and all that must be added is a dissipation function for the non-conservative elements,

$$D = \frac{b}{2}\dot{u}_{2L}{}^2 + \frac{b}{2}\dot{u}_{2R}{}^2 + \frac{1}{2R}\dot{\lambda}^2, \tag{4.25}$$

where b is the dissipation constant for the mechanical system and R is the electrical resistance. By taking the various derivatives for the Lagranges equations, we can write the full equations of motion describing the electromechanical coupling between the piezoelectric circuit and the two half beads,

$$m\ddot{u}_{2L} + b\dot{u}_{2L} = -nd_{33}K_a\dot{\lambda} + K_a(u_{2R} - u_{2L}) + A(\delta_0 - u_{2L} + u_1)^{\frac{3}{2}} \\ + b\dot{u}_{2L}$$

$$m\ddot{u}_{2R} + b\dot{u}_{2R} = nd_{33}K_a\dot{\lambda} - K_a(u_{2R} - u_{2L}) - A(\delta_0 - u_3 + u_{2R})^{\frac{3}{2}} \\ + b\dot{u}_{2R} \tag{4.26}$$

$$C(1 - k^2)\ddot{\lambda} + nd_{33}K_a(\dot{u}_{2R} - \dot{u}_{2L}) + \frac{\dot{\lambda}}{R} = 0.$$

These equations of motion fully define the electromechanical coupling. By looking at the mechanical equations of motion it is clear that the circuit acts as an energy sink. When this damping is on the order of the mechanical damping then it may have a significant effect. Inductive damping occurs when there is an additional inductor placed in series with the resistance[99]. This leads to a modified Lagrangian, $L = T - V + W_e^* - W_m$, where $W_m = \lambda^2/2L$ is the energy stored in the inductor. The resulting RCL circuit (and equations of motion) now has its own resonance and can be tuned to couple more or less with the mechanical system.

4.5   Modeling for specific experiments

4.5.1   Local to extended transitions of resonant defect modes

This modeling is for the experimental setup described in section 3.3.1. The results are shown in chapter 5. We model our system as masses coupled by springs with a single defect site. All particles other than the defect are spherical with $R = 9.525 \, mm$ and a mass, $m_s = 28.8 \, g$. The equations of motion are,

$$m_s \ddot{u}_i = k_c (u_{i+1} + u_{i-1} - 2u_i); \quad i \neq 0$$
$$m_0 \ddot{u}_0 = k_c (u_1 + u_{-1} - 2u_0) + k_R (u_r - u_0) \tag{4.27}$$
$$m_r \ddot{u}_r = k_r (u_0 - u_r),$$

where u_i is the displacement of the ith sphere around its equilibrium position. The equations represent a one-dimensional lattice with a local resonance at the defect site. The defect's dynamics are contained in the second two equations, and the rest of the lattice in the first. The defect has a mass located in the chain array, which is $m_0 = 47.8 \, g$, and has a displacement from equilibrium, u_0. The defect's resonant mass, $m_r = 0.18 \, g$, is coupled with a stiffness, $k_r = 2.64 \times 10^5 \, N/m$, to this particle and has a displacement, u_r. This displacement is the additional degree of freedom for the resonator. We define the characteristic frequency of the resonator, $f_r = \sqrt{k_r/m_r}$, which is totally independent of the lattice, and we stress that this is not equal to the defect mode's frequency. The stiffness coupling of all other particles within the chain is found by linearizing the Hertzian contact law, $k_c = \frac{3}{2} A^{2/3} F_0^{1/3} \left[\frac{N^{2/3}}{\mu m} \right]$, where F_0 is the compression, $A = \frac{4}{3} \sqrt{\frac{R}{2}} \left(\frac{E}{2(1-\nu^2)} \right)$, $E = 193 \, GPa$, and $\nu = 0.3$. This is where the

nonlinear nature of our lattice is important. This allows a change in the coupling stiffness

between adjacent particles through compression, while the resonant coupling stiffness, k_r,

stays constant. Finally, the boundary conditions are modeled as fixed walls with $u_{-16} = u_{16} =$

0.

The dynamics we are interested in are linear, and therefore we solve the eigenvalue problem

that results from assuming oscillatory solutions. In section 5.4 we show our analytical

derivation, which is used to fit for experiments and demonstrates that boundary conditions do

not become important until just before the mode transitions from local to extended dynamics.

4.5.1.1   Modeling the resonant defect

The resonant defect is essential to our investigation of actively controlled localization, and the

defect itself is modeled as two separate parts. To characterize the defect's behavior, we

perform a separate experimental and numerical analysis. A portion of the defect particle's

mass, m_0, is localized in the lattice array and coupled to the other particles through the same

nonlinear Hertzian Contact. Another part of the mass, m_r, is in the resonating ring. This mass

is determined using Finite Element simulations in Comsol Multiphysics®. The spring

constant, $k_r = m_r f_r^2$, coupling the masses is calculated using the linear mode's frequency, f_r.

This frequency is found by measuring the transmission properties of a single resonator where

the frequency f_r is the anti-resonance. A schematic of the experimental setup is shown in Fig

4.3a, with the transmission spectra shown in Fig 4.3b. The blue curve plots the experimental

results, and the red curve is the corresponding numerical results from a linear state space
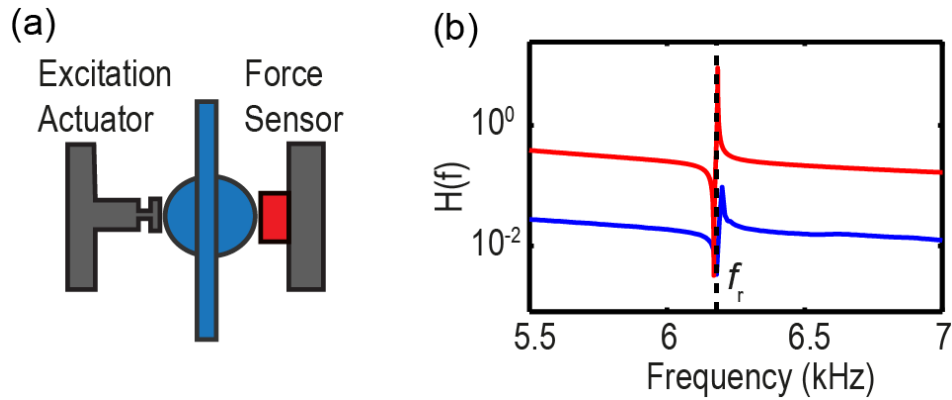
analysis.

Figure 4.3: Experimental Analysis of the Resonant Defect Particle. (a) The schematic of the experimental characterization system. (b) A comparison between the theoretical and experimental transmission spectra for the system in (a).

4.5.2   Extraordinary stiffness tunability

This modeling is for the experimental setup described in section 3.3.2. The results are shown in chapter 6. We use a discrete particle model to simulate the dynamics. The table below lists the values used in the simulations, which are either measured experimentally or fit for. We fit for two parameters in our model.

The first is the lattice's Hertzian contacts at the ends. We found that the experimental support expands slightly as a result of its finite stiffness. We include this by modifying the contacts at the edges of the chain, A_1 and A_{10}. This does not affect the dynamics at the defect site. Figure 4.4 shows the Hertzian fit used to find the total stiffness of the chain and supporting structure,.

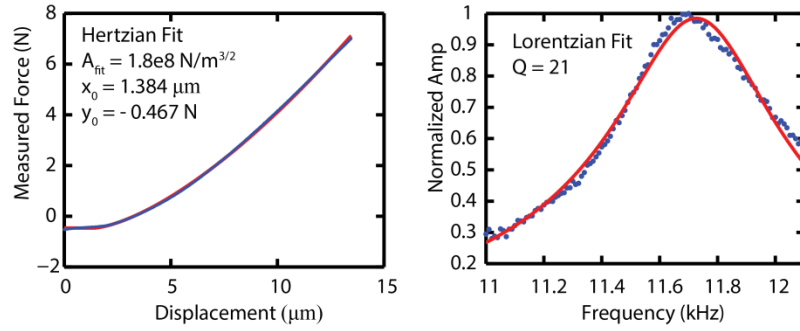$$A_{fit}^{-2/3} = \sum_i A_i^{-2/3}.$$ (4.28)

Figure 4.4: Experimental Fits to determine Numerical Parameters. (Left) Fit of the static response of the chain to Hertzian Force Law. (Right) Fit of the linear amplitude response of the defect to a Lorentzian to determine the linear dissipation of the chain.

The second we fit for is the linear dissipation of the particles. To find this we perform a frequency sweep at low amplitude drive excitations in the experiment and fit the measured amplitude response to a Lorentzian. We measure the quality factor of the mode and then choose a dissipation time constant for the numeric that results in the same quality factor for the defect mode.

The contacts at the excitation particle are modified to include the sinusoidal expansion of the chain. Because the stiffness of the piezoelectric disk is much larger than the Hertzian contacts, the piezo expands in proportion to the voltage applied, and the assembled structure can be assumed to move as a single expanding bead.

$A_i = 9.7576 \ N/\mu m^{3/2}, \quad i \neq 1,5,7,10$	Sphere – sphere contact stiffness
$A_1 = A_{10} = 1.7106 \ N/\mu m^{3/2}, \\ i = 1,10$	Boundaries contacts stiffness
$A_5 = 7.9670 \ N/\mu m^{3/2}$	Defect sphere contact stiffness
$A_7 = 13.799 \ N/\mu m^{3/2}$	Excitation particle – sphere contact stiffness
$m_i = 28.4 \ g, \quad i \neq 6,7$	Sphere mass
$m_6 = 3.6g, \quad m_7 = 20.2g$	Defect mass, and excitation particle mass

$\delta_i = \left(\dfrac{F_0}{C_i}\right)^{2/3}, \qquad i \neq 6,7$	Equilibrium spatial overlap
$\delta_i = \left(\dfrac{F_0}{C_i}\right)^{2/3} + \dfrac{B}{2}\cos(2\pi f_d t),$ $i = 6,7$	Spatial overlap including the harmonic signal applied to the excitation particle
$\tau = 0.275ms$	Dissipation time constant

Table 4.2: Model Parameters (A_1, A_{10}, masses, τ are experimentally measured).